Cell Reports
Physical Science

CellPress
OPEN ACCESS

Article

Dynamic residual deep learning with photoelectrically regulated neurons for immunological classification

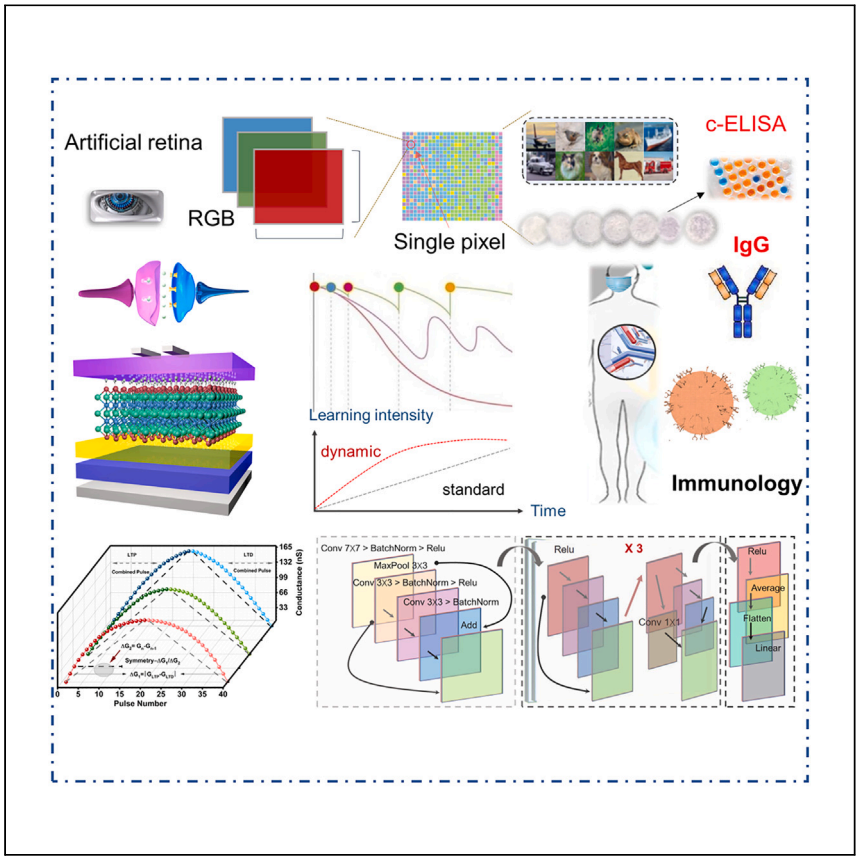

Wang et al. construct a photoelectrically regulated synaptic transistor to adjust the nonlinearity and asymmetry by mixing controllable pulses. Combined with the residual network, this device can achieve immunological classification. Dynamic update rule of weight iteration processes can also extend standard datasets.

Qinan Wang, Sixuan Duan, Jiahao Qin, ..., Xin Tu, Hao Gao, Chun Zhao

pengfei.song@xjtlu.edu.cn (P.S.)
wen.liu@xjtlu.edu.cn (W.L.)
chun.zhao@xjtlu.edu.cn (C.Z.)

Highlights

The synaptic MXene transistor has high symmetry of LTP/LTD

Dynamic learning improves the accuracy of a highly similar and homologous database

LSTM, Cifar10, and Cifar100 prove the strong robustness

Wang et al., Cell Reports Physical Science 4, 101481
July 19, 2023
https://doi.org/10.1016/j.xcrp.2023.101481

Cell Reports
Physical Science

CellPress
OPEN ACCESS

Article

Dynamic residual deep learning with photoelectrically regulated neurons for immunological classification

Qinan Wang,[1,2] Sixuan Duan,[1,2] Jiahao Qin,[3] Yi Sun,[1,2] Shihang Wei,[1,2] Pengfei Song,[1,*] Wen Liu,[1,*] Jiangmin Gu,[1] Li Yang,[3] Xin Tu,[2] Hao Gao,[4] and Chun Zhao[1,5,*]

SUMMARY

Dynamic deep learning is considered to simulate the nonlinear memory process of the human brain during long-term potentiation and long-term depression. Here, we propose a photoelectrically modulated synaptic transistor based on MXenes that adjusts the nonlinearity and asymmetry by mixing controllable pulses. According to the advantage of residual deep learning, the rule of dynamic learning is thus elaborately developed to improve the accuracy of a highly homologous database (colorimetric enzyme-linked immunosorbent assay [c-ELISA]) from 80.9% to 87.2% and realize the fast convergence. Besides, mixed stimulation also remarkably shortens the iterative update time to 11.6 s as a result of the photoelectric effect accelerating the relaxation of ion migration. Finally, we extend the dynamic learning strategy to long short-term memory (LSTM) and standard datasets (Cifar10 and Cifar100), which well proves the strong robustness of dynamic learning. This work paves the way toward potential synaptic bionic retina for computer-aided detection in immunology.

INTRODUCTION

The in-memory computing framework as the core part of the synaptic device has been an exciting subject for machine learning of artificial intelligence. Traditional computer systems based on von Neumann architecture have the disadvantage of high energy consumption.[1,2] The remarkable intellectual abilities of the human brain, including learning and memory, stem from an intricate network of almost 100 billion neurons linked together by synapses.[3] The adaptive capability of a synapse to modify its connection strength, also known as synaptic plasticity, is crucial in facilitating learning and memory.[4] Additionally, neuronal intrinsic plasticity occurs simultaneously with synaptic plasticity in all key forms of learning, enabling the brain to perform intelligent tasks and probabilistic processing with remarkable efficiency while consuming low energy.[5] Furthermore, it is essential to explore and combine neural devices that conform to the memory rules of the human brain. In order to achieve multilevel storage and parallel computing in the neural network, synaptic transistors composed of metal oxide, two-dimensional materials, organics, and photoelectricity materials have been proposed recently for simulating synaptic plasticity.[4–7] According to the various mechanisms of nonvolatile devices, floating-gate transistors (charge trapping), ferroelectric-gate transistors (spontaneous polarization states), electrolyte-gate transistors (ion migration), and optoelectronic transistors (photogenerated carrier) are applied to the neural computing. Most research focuses on artificial intelligence of neuromorphic computing about supervised

[1]School of Advanced Technology, Xi'an Jiaotong-Liverpool University, Suzhou 215123, China

[2]Department of Electrical Engineering and Electronics, University of Liverpool, Liverpool L69 3GJ, UK

[3]School of Science, Xi'an Jiaotong-Liverpool University, Suzhou 215123, China

[4]Department of Electrical Engineering, Eindhoven University of Technology, Den Dolech 2, 5612 AZ Eindhoven, the Netherlands

[5]Lead contact

*Correspondence:
pengfei.song@xjtlu.edu.cn (P.S.),
wen.liu@xjtlu.edu.cn (W.L.),
chun.zhao@xjtlu.edu.cn (C.Z.)

https://doi.org/10.1016/j.xcrp.2023.101481

learning (artificial neural network and convolution neural network) and unsupervised learning (cluster and self-adaptive organization).[5–9]

Applying stimulation (electric pulse, optical pulse, or stress) to the pre-synaptic terminal simulates the realization of synaptic plasticity for the bionic nerve. The stability and controllability of the storage process has to be strengthened, despite the results of optoelectronic hybrid mode's significance.[10,11] Moreover, the dimension of materials influences transmission efficiency and data processing when the synaptic devices are integrated for parallel computing. A comprehensive modulation of mixed photoelectric pulses for long-term depression (LTD) and long-term potentiation (LTP) has been lacking in recent years.[12,13] Furthermore, the fundamental symmetry and linearity of conductance in the rising and falling stages during the algorithm of error feedback is also not properly considered for their impact on accuracy, and the weight updating process is merely simulated in accordance with the fitted LTP/LTD curves. In previous research, the standard case (LTP/LTD are two straight lines) is generally adopted as the learning step size in each iterative epoch.[14] Afterward, inspired by the first impression of human cognition, the relationship between learning efficiency and temporal memory is nonlinear. In other words, a great amount of accurate information can be retained, and learning is generally particularly efficient in the early stages.[8] The difference in conductance (ΔG) between two synaptic transistors is normalized to represent the synaptic weight connection strength of two neural units due to the weight range in the neural algorithm containing the negative value.[7] Consequently, the convex function composed of LTP/LTD curves can provide a tight connection strength at the initial epoch of training, and the strength gradually decreases with the increase of the number of iterations.[6–9] According to each nonfixed stage on the curve, the proposed dynamic learning rule provides the mapping relationship between the dynamic learning step and the epochs. The one-to-one symmetry of conductance in the potentiation and depression stages, in addition to the nonlinearity, assists the dynamic response of neuromorphic computing.[13] The iteration direction of synaptic weight is based on the Manhattan rule in the error backpropagation. Therefore, the updated trend of nonmonotonicity requires strong symmetry of LTD/LTP. The strength of symmetry is then suggested to be measured by the ratio of $\Delta G_1/\Delta G_2$.[15–17] Previous research has shown that conventional neural networks (such as artificial neural networks [ANNs] and convolutional neural networks [CNNs]) are unable to accomplish indistinguishable categorization tasks due to degradation, which is also the challenge in deep neural networks.[13–20] The residual learning framework is proposed to simplify the training of networks that are substantially deeper than those previously used. The layer as the learning residual function is explicitly redefined by the reference layer instead of the learning datasets with labels compared with the ANN and CNN.[16] Besides, the differences between various tags are amplified as network layers increase, making it easier to distinguish between tags with a high level of similarity. Further, the immunology colorimetric enzyme-linked immunosorbent assay (c-ELISA) image data format fully complies with the requirements of high similarity. As the most widely used technique in immunoassays, c-ELISAs based on microfluidic paper-based analytical devices (μPADs) are the gold standard for detecting protein biomarkers in disease-related clinical samples and can be applied to detect diseases such as human immunodeficiency virus (HIV), COVID-19, Lyme disease, etc.[21,22] Then, in recent years, μPADs as one kind of point-of-care (POC) diagnostics have received a lot of attention for their ability to perform rapid, real-time on-site testing in nonlaboratory settings and provide accurate diagnostic results.[23,24] Especially, the c-ELISA produces color signals that are correlated with the specific binding of the enzyme-labeled antibody to the sensing target molecule, with high color signals

representing high concentrations of sensing target molecules. These color signals can be easily picked up by the naked eye or by smartphones without the need for more sophisticated equipment.[25,26] However, the differences in color signals displayed by different concentrations of sensing target molecules are not obvious, especially at low concentrations.[27,28] Therefore, the ability to effectively distinguish color signal differences of sensing target molecules remains an urgent requirement to improve the performance of colorimetric μPAD analysis. Consequently, this problem can be well solved by using a two-dimensional (MXene) synaptic transistor combined with dynamic learning strategies in residual neural networks.

In this article, we for the first time report a deep residual learning strategy based on dynamic rules and Al/InO_x/MXenes/ZrO_x-Li/Si/Al structure. The nonlinearity and symmetry of LTP/LTD trends are successfully modulated by adopting the proposed three applied pulse modes (type I [electrical stimulation], type II [light stimulation], and type III [combined stimulation]). Further, we construct datasets by using the classic rabbit immunoglobulin G (IgG) antigen as the c-ELISA sensing target for the identification task. The feasibility of combining a dynamic deep neural strategy with synaptic transistors is explored by analyzing image results of seven different concentrations of c-ELISA for rabbit IgG. The combined stimulation can obviously improve the standard accuracy (fixed learning rate) and shorten the update time in neuromorphic computing. The robustness of dynamic tracking rules under different training structures (ResNet and LSTM) and different classification tasks (ELISA, Cifar10, and Cifar100) are further analyzed to verify the advantages of combined stimulation. Finally, the bionic retina combined with the dynamic neuromorphic residual deep learning strategy is successfully implemented by adopting a highly homologous database of immunology. This mainly depends on the high nonlinearity and symmetry after photoelectric hybrid control, which effectively shortens the number of neural network training epochs. Meanwhile, the high homology of c-ELISA also further highlights the advantages of residual deep learning, which well matches the synaptic plasticity of the device to practical applications.

RESULTS AND DISCUSSION

The connection between synaptic transistor and biological functions

The human brain processes external information mainly through various senses and perceptions—most behaviors and decisions from neurons and synapses are based on the visual receptor. Pyramidal cells and the optic nerve are connected one to one, distinguishing short-wave, middle-wave, and long-wave lights (Figure 1A). Artificial retina based on the synaptic devices identify RGB values from a single pixel.[29–32] The c-ELISA is the gold standard in immunoassays for the quantitative detection of antibodies, antigens, proteins, hormones, etc. (Figure 1B). Also, c-ELISA can be widely used for rapid antibody screening tests for viruses (HIV, COVID-19 virus, etc.), autoimmune diseases, progesterone HCG, laboratory and clinical studies, and other diagnostics. Figure 1C shows the schematic diagram of a direct c-ELISA performed in a μPAD and the image results of seven rabbit IgG concentrations (0, 6.7 pM, 67 pM, 670 pM, 6.7 nM, 67 nM, and 670 nM). The specific experimental steps will be described in the experimental procedures. To achieve the application of immune protein detection in immunology, the Al/InOx/MXenes/ZrOx-Li/Si/Al structure is designed to achieve synaptic plasticity by simulating the internal linkage between the learning speed and non-volatile conductance through the combined pulse control (Figure 1D). Compared with the bionic neural network created using the von Neumann architecture and CMOS (complementary metal oxide semiconductor) process currently available,

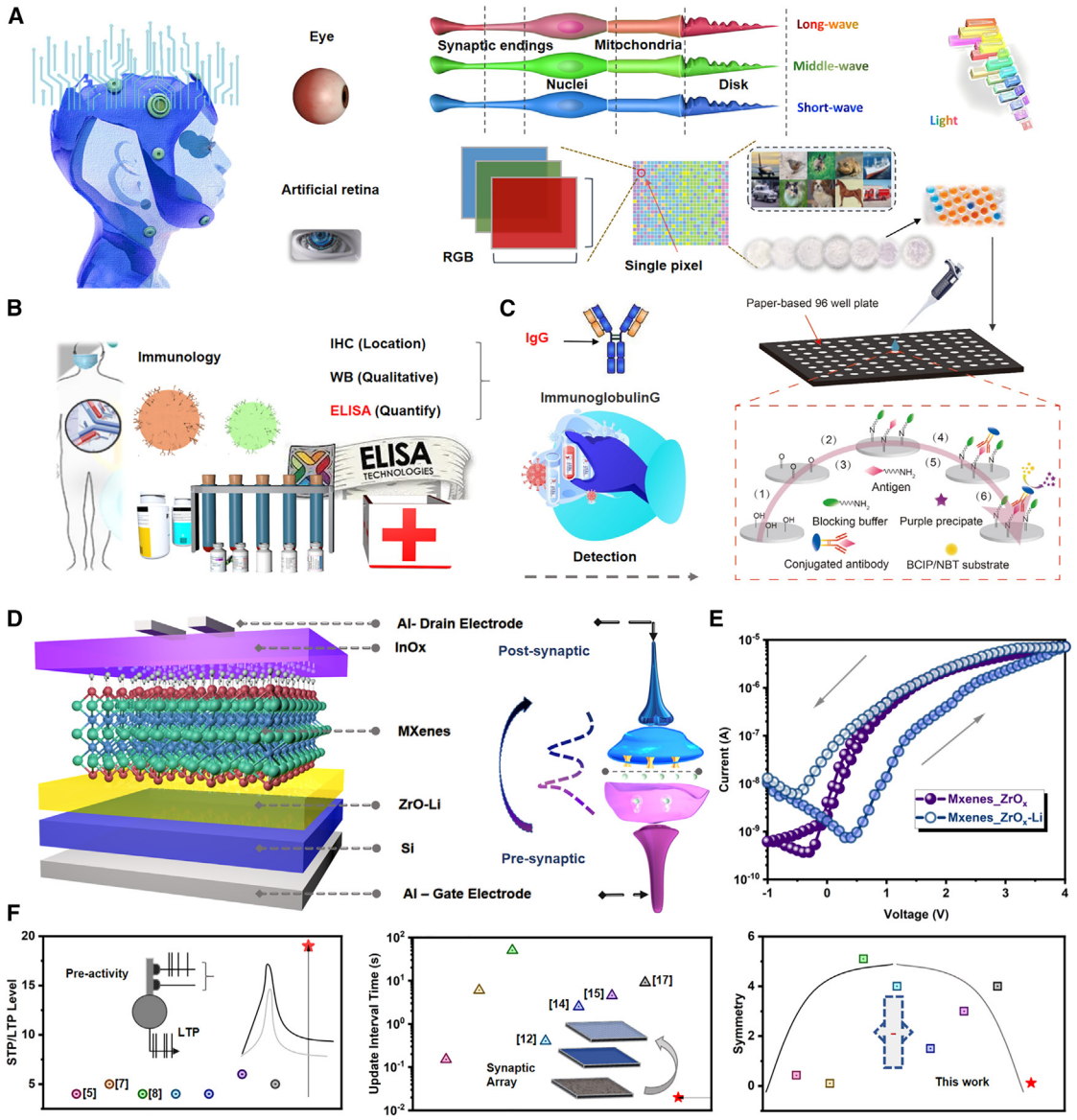

Figure 1. Real application scenarios of neuromorphic computing and the structure and advantage of the proposed synaptic device

(A) Schematic diagram of the visual receptors accepting light stimulation through three kinds of cone cells.

(B) Significance of c-ELISA in immunology and its detection methods.

(C) Schematic diagram of a direct c-ELISA performed in a μPAD and the image results of seven rabbit IgG concentrations (0, 6.7 pM, 67 pM, 670 pM, 6.7 nM, 67 nM, and 670 nM).

(D) Schematics illustrate the biological synapse and the Al/InO$_x$/MXenes/ZrO$_x$-Li/Si/Al synaptic transistor.

(E) Transfer characteristics with and without Li^+ ion doping transistors.

(F) Competitive indicators of synaptic transistor for STP/LTP level, update interval time, and symmetry.

synaptic devices offer more efficient parallel processing speeds and lower energy consumption when dealing with complex tasks. The two-dimensional material depends on the short ion transport distance, excellent electron transport dynamics, and photoelectric response to compose the part of synaptic transistors.[33] Compared with the organic materials and metal-oxide materials as the partial structure of synaptic transistors, two-dimensional materials have the advantage of simple technology, high product yield, fast electronic transmission speed, and stability in environmental change.[34–36] The clear layered structure is observed by

scanning electron microscopy (SEM) (Figure S1). The X-ray diffraction spectrum for $Ti_3C_2T_x$ MXenes presents a small peak of 6.4°, typical of MXenes (Figure S2). The Ti 2p X-ray photoelectron spectroscopy spectra of MXene demonstrate the apparent peaks of TiO_2 ($2p_{3/2}$) and TiO_2 ($2p_{1/2}$) due to the oxidation during the InO_x fabrication process (Figure S3). In previous studies, optoelectronic synaptic transistors have had the advantages of large bandwidth, low energy consumption, and ultrafast signal transmission for ANNs and retina. For the weight update process that has been widely employed in previous studies, neural computing adopts one of the LTP/LTD curves through the light stimulated or electrically stimulated pulses. To tackle the limitations of the nonlinearity extracted from conductance and the single update rule adopted, the double dynamic update rule is developed according to the ΔG when the pre-terminal is stimulated by electric pulse and mixed pulse. The schematic diagram of the synaptic transistor and synapse demonstrates the gate electrode as the pre-synaptic terminal and the drain electrode as the postsynaptic terminal. The transmission of information in the synapse is that the chemical signals are converted into electrical signals when the synaptic vesicles release neurotransmitters.[33,34] To verify the synaptic plasticity, the transfer characteristic curves with Li^+ doped into the ZrO_x layer (5% doping concentration) demonstrate the large hysteresis of typical synaptic characteristics (Figure 1E), and this phenomenon benefits from achieving multilevel storage. Furthermore, the transfer characteristics of an undoped transistor have no evident hysteresis, clarifying that Li^+ ion migration changes the channel conductance. To briefly explain the transformation from short-term potentiation (STP) to LTP and the dynamic update decision, the schematic diagram shows the mechanism when an electric pulse and an optical pulse are applied to the gate and channel, respectively. When a positive voltage is applied to the pre-synaptic terminal, Li^+ ions with a large diffusion coefficient and small atomic radius will migrate from the ZrO_x layer to the MXenes and semiconductor layer with the increase of voltage amplitude. For applying the optical pulse at the channel (photon radiation: $V_O + h\nu \rightarrow V_O^{2+} + 2e^-$), the oxygen vacancies in the metal-oxide network generate the electron-hole pairs (Figure S4). The competitive advantages of this work are the update interval and the symmetry of LTP and LTD.[4–8,11–20] Figure 1F summarizes the competitive indicators just mentioned in the past 4 years and concludes that energy consumption can be saved and synaptic plasticity can be improved.[5,7,8,12,14,15,17]

Electric pulse and light pulse make devices produce synaptic plasticity and biological characteristics

To verify the synaptic plasticity of the transistor, the nonvolatile conductance is recorded when optical and electrical pulses are applied to the channel and the presynaptic terminal, respectively.[35] The paired-pulse facilitation (PPF) preliminarily shows short-term synaptic plasticity, which is the basic function of a biological synapse for processing temporal information (Figure 2A). The interval time (Δt) between pulses increases from 20 to 1,000 ms and the amplitude of electric pulses from 0.5 to 1.5 V with each increase of 0.25 V. The expression of the PPF index depends on the ratio of the first and second peak values (A_2/A_1) of the excitatory postsynaptic current (EPSC). The PPF fitting curves include the initial constants (C_0, C_1, and C_2) and the relaxation times (τ_1 and τ_2) that describe the convergence rate and downward trend (Figure S5B). The highest PPF index of Δt = 20 ms is attained by the appropriate voltage stimulation (1 V), and the parameters of the fitting curve are about C_0 = 1, C_1 = 35%, C_2 = 48%, τ_1 = 35 ms, and τ_2 = 35 ms. Similarly, the PPF index curve (C_0 = 1, C_1 = 28%, C_2 = 36%, τ_1 = 22 ms, and τ_2 = 56 ms) stimulated by blue light also shows synaptic plasticity when the

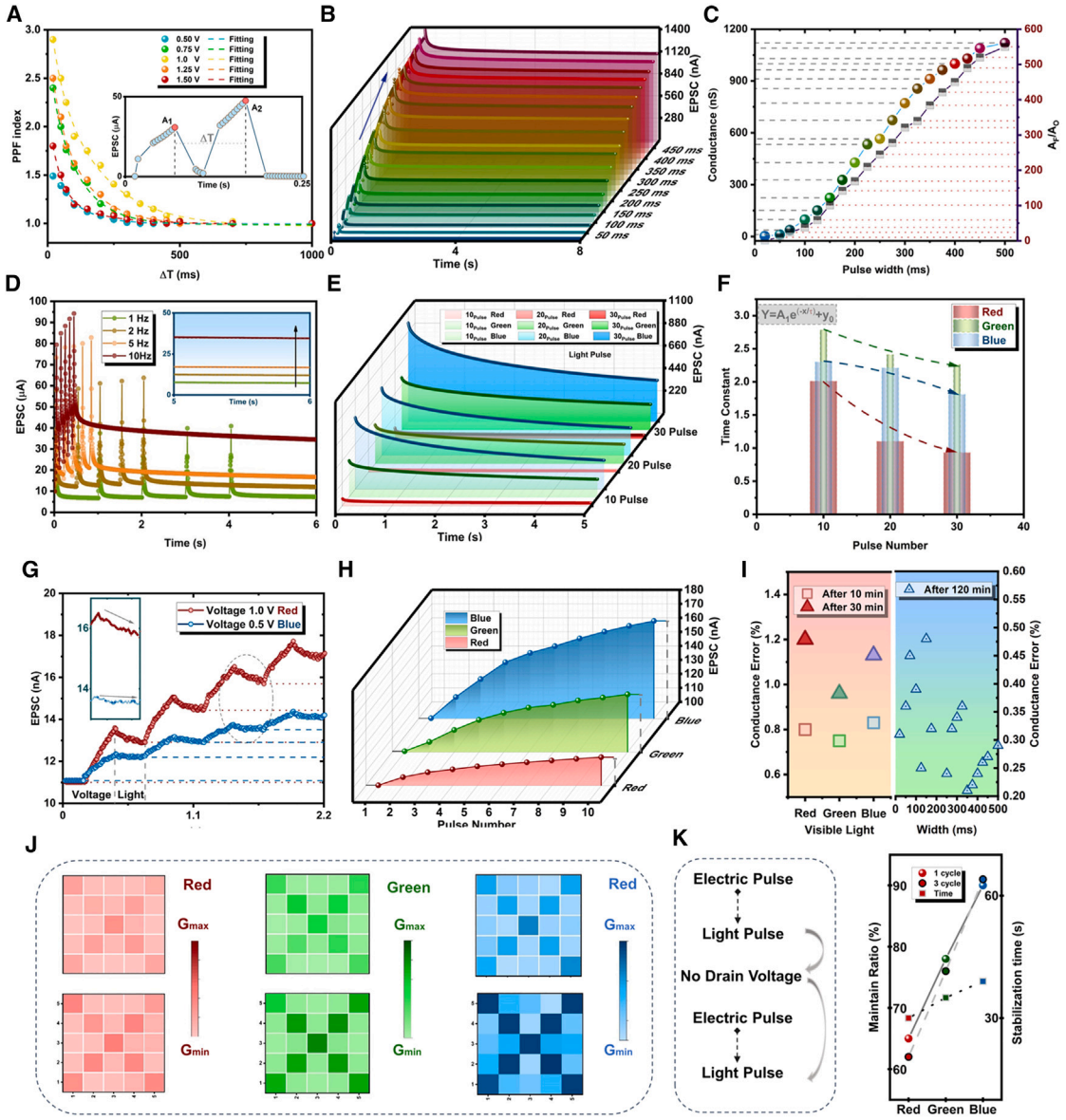

Figure 2. Synaptic plasticity and nonvolatility after pulse stimulation with different parameters

(A) PPF index versus interval time Δt under various voltage amplitude (0.50, 0.75, 1, 1.25, and 1.50 V). Inset: definitions of A_2 and A_1 with two successional 50 ms pulses.

(B) EPSC triggered by 19 single pulses with different durations (20, 50, 75, 100, 125, 150, 175, 200, 225, 250, 275, 300, 325, 350, 375, 400, 425, 450, 475, and 500 ms) at V_{DS} = 0.5 V

(C) Extracted stable conductance for various pulse widths and the ratio of stimulated conductance over initial conductance (A_F/A_O).

(D) EPSC stimulated by five continuous electric pulses (1 V, 40 ms) with different frequencies (1, 2, 5, and 10 Hz).

(E) Relaxation process of EPSC stimulated by the different numbers of red, green, and blue pulses (10, 20, and 30).

(F) Time constant extracted from the natural forgetting process.

(G) EPSC triggered by two mixed pulses (0.5 V + blue and 1 V + red), which means the electric pulse combined with the optical pulse.

(H) LTP stimulated by ten groups of light pulses that involved red, green, and blue optical pulses, respectively.

(I) Errors of conductance under electric and combined pulses modulated (after 30 and 300 min).

(J) Three 5 × 5 matrices for demonstrating the change of conductance of the cycle of 1 and 3 combined pulses.

(K) Maintain ratio and stabilization time for 1 and 3 cycles.

photoelectric effect occurs in the channel (Figure S5A). Further, the conversion from short-term to long-term synaptic plasticity is obtained by increasing the electric pulse width to 500 ms (Figure 2B). The 19 initial conductance values increased from 14.9 nA (Figure S6). This phenomenon is attributed to the Li^+ ion migration in the ZrO_x and MXene layers, leading to multiple conductance states.[36] With the width increasing linearly, the changing trend of 19 levels tends to be linear, proving that the conductance is precisely programmed by the electrical pulse width (Figure 2C). The (ZrO_x/MXenes) without Li doping has no STP-LTP response of synaptic plasticity according to the EPSCs. This phenomenon further proves that the Li^+ ion plays an irreplaceable role in the channel conductance update for neuromorphic computing and that common ZrO_x gate dielectrics are not adequate for a large retention range (Figure S7). Further, to verify the low energy consumption of the synaptic device, the energy consumption per spike of syanptic transistor is calculated by the equation $E = I_{peak} \times t \times V = 80.19$ pJ (Figure S8). I_{peak} is the maximum value (80.19 nA) of the generated EPSC curve, t is the spike duration (20 ms), and V is the voltage applied to the drain electrode (0.05 V). Similarly, pulse frequency (1, 2, 5, and 10 Hz) also affects the conductance observed from the EPSC curves. Five consecutive pulses stimulated these curves with the same parameters (1 V and 40 ms), except for frequency (Figure 2D). The inset of Figure 2 demonstrates the obvious multiconductance and stable nonvolatile value within 6 s. On the other hand, to research the optically controlled synaptic plasticity, three wavelengths of light (red, green, and blue) are applied to the InO_x and MXene layers. Compared with electrical plasticity, the photocurrent can also be accumulated through the superposition of the number of pulses. The main photoelectric response of MXene under the light with three wavelengths (red = 680 nm, green = 540 nm, and blue = 490 nm) causes a long relaxation time (Figure 2E). Light with a small wavelength carries strong photon energy, which excites a high photocurrent. Analysis of the relaxation process based on the time constant ($\tau_{10} = 1.91, \tau_{20} = 1.08, \tau_{30} = 1.08$) illustrates that the fastest decay rate belongs to red light (Figure 2F). This phenomenon provides potential feasibility for combined pulse stimulation, which means that optical pulses and electric pulses are used alternately during conductance updates.[37] According to previous research, one of the drawbacks of the synaptic transistor (memory) is conductance decay. There is always a trade-off between computing speed and accuracy. In short, if the computing speed is fast, then extensive decay will significantly increase the error. The combined pulses are adopted to shorten the decay process and maintain the conductance state to solve this bottleneck. The first step is to apply an electrical pulse (0.5 V) to the pre-synaptic terminal, and then an optical pulse (blue) is applied to the channel (Figure 2J). Maintaining the peak conductance value can be observed from the EPSC trend compared with the red pulse. The benefit is to accelerate the conductance update speed greatly. Afterward, the same pulse combination rule is extended to red, green, and blue pulses, with the electric pulse amplitude being 0.5 V (Figure 2H). After ten cycles of combined pulses, the conductance values of the three conditions for adding red, green, and blue pulses are 11.5, 13.2, and 16.3 ns, respectively. In addition, as a synaptic device for neuromorphic computing, nonvolatile conductance is also a necessary factor.[38] To demonstrate all aspects of stability, the conductance errors are counted in three states (10, 30, and 120 min later) after stimulation by ten combined pulses (Figure 2I). The error range for combined pulses floats between 0.7 and 1.2, satisfying the storage and computing requirements for the neural network. Similarly, the conductance controlled by the gate can hold relatively stable after 10, 30, and 120 min as a result of a 0.25%–0.60% error range. To demonstrate the high level of stability, the variances between the initial conductance and

the conductance maintained after 300 and 600 min are compared, and the results indicate that the majority of errors are below 0.5% (Figure S9). Due to all results of Figure 2, the Al/InO_x/MXenes/ZrO_x-Li/Si/Al synaptic transistor has a variety of stable modulation modes. To further verify the feasibility of large-scale integration, the combined pulse update rule applied in a single device is extended to the 5 × 5 matrix (Figure 2J). The electric pulse amplitude in all combined pulses is 0.5 V, and the pulse width is 50 ms. When the combined pulses are the electric pulse and blue pulse, the ratio of the peak value over the stable value reaches 91%, and the relaxation time is shorter than the other combinations (Figure 2K). The short relaxation time enormously curtails the interval between each weight update for the neural network.[39] Every two 5 × 5 matrices demonstrate the conductance distribution in two states (after one cycle and three cycles), and one cycle represents the complete stimulus of the combined pulses. In addition, the conductance value after receiving circulatory stimulation can still maintain 99% of the stable value within 30 s. Therefore, the above results provide novel and efficient rules for simulating the weight updating process in the neural network.

Simulated weight update process relies on potentiation and depression under three modes of stimulation

Replacing the weight matrix in a neural network with a synaptic device matrix is indispensable for developing neural morphological electronics.[40] The update rules of the simulated weight matrix apply the periodic trend of LTP/LTD in the synaptic transistor. The mode of pulses applied for three types (type I, type II, and type III) are positive pulse/negative pulse, optical pulse/negative pulse, and combined pulse/combined pulse, respectively (Figure 3A). The parameters extracted by LTP/LTD curves and applied to the neural calculation are G_{max}/G_{min}, nonlinearity, cycle-to-cycle error, and symmetry. Then, the modification of G_{max}/G_{min} and nonlinearity by electric pulse amplitude and pulse number in type I is researched. When the number of pulses is 100, the number of conductance updates increases, resulting in a larger ratio of G_{max}/G_{min}. Further, when the voltage amplitude increases from 0.5 to 1.25 V in a step of 0.25 V, the number of pulses required becomes small and makes the conductance reach relative saturation, resulting in the curve fitting into a convex function gradually (Figure 3B). The range and resolution of the weight update process depend on the G_{max}/G_{min} ratio, the learning step size of each epoch depends on the nonlinearity and symmetry of LTP/LTD, and the stability of training and testing depends on the cycle-to-cycle error.[41] Above, all factors together affect the final classification accuracy. The cyclic stability of LTP/LTD is verified by alternately applying the positive (0.5 V, 40 ms) and negative (−0.5 V, 40 ms) electric pulses to the pre-synaptic terminal. With the increase in the number of pulses (20, 30, 40, and 100), the cycle-to-cycle errors rise to 1.31%, 1.56%, 1.36%, and 1.33% after ten cycles, respectively (Figure 3C). The errors floating within a specific limit show the robust stability of LTP/LTD, which benefits the training and test process. During the update process, three update modes are proposed to demonstrate the influence of the electric pulse and optical pulse on parameters extracted from the LTP/LTD curve. Then, the modification of G_{max}/G_{min} and nonlinearity by electric pulse amplitude and pulse number in type I is researched. When the number of pulses is 100, the number of conductance updates increases, resulting in a larger ratio of G_{max}/G_{min}. Moreover, the ΔG between the two synaptic transistors (G^+ and G^-) is used to represent the weight range (−1 to 1) in the algorithm (Figure 3D). Notably, the left and right parts of the curve need to match the symmetry because the rising and falling stages of conductance should have one-to-one correspondence.[42] To explore the regulation of the optical pulse on nonlinearity and symmetry, type II and type III are developed. The curvature of

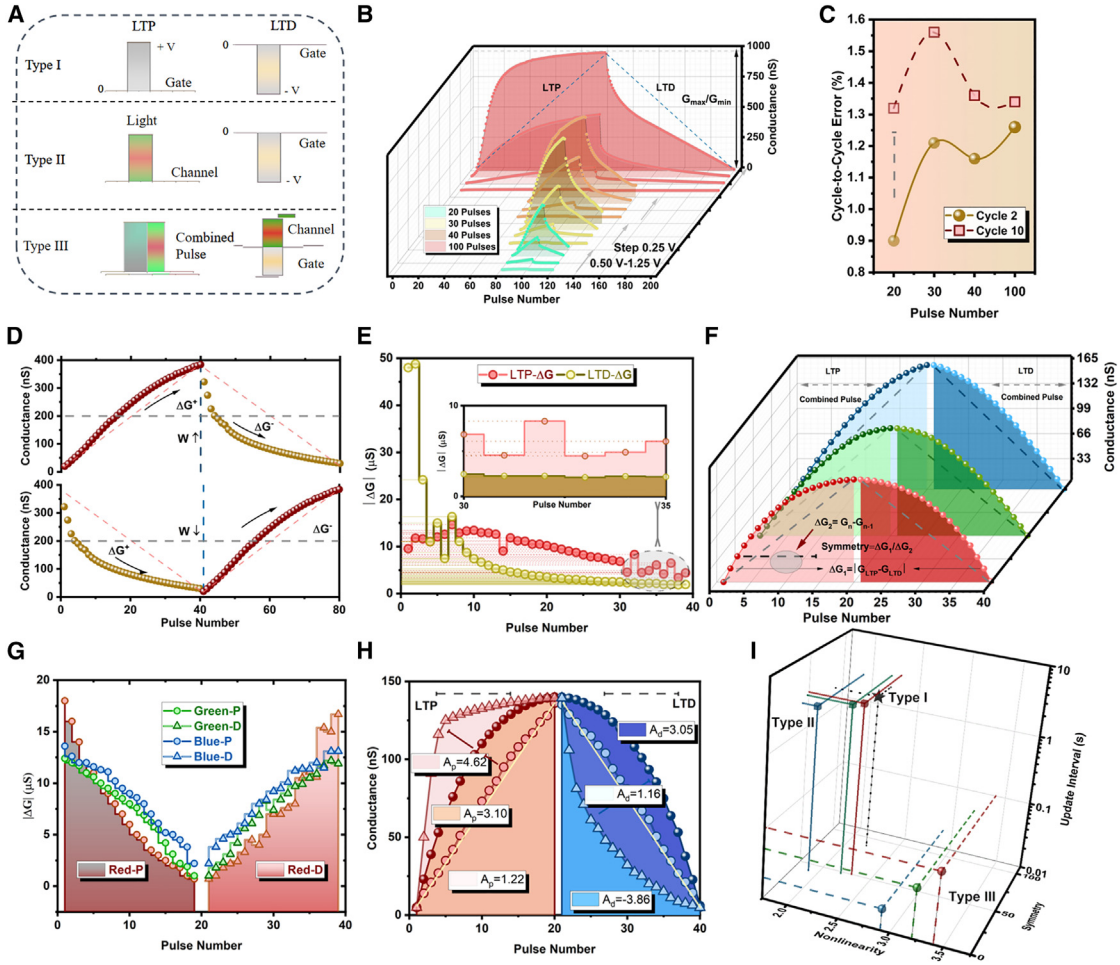

Figure 3. Nonlinearity and symmetry in trends of LTP/LTD are regulated by three types of pulses

(A) Illustration of three types (type I, type II, and type III): positive pulse/negative pulse, optical pulse/negative pulse, and combined pulse/combined pulse.

(B) LTP/LTD curves for various electric pulse numbers under the incremental pulse amplitude from 0.50 to 1.25 V

(C) Conductance cycle-to-cycle error for different pulse numbers.

(D) Synaptic weight update rule of two synaptic transistors (G^+ and G^-) for the above three types.

(E) Change trend of ΔG in LTP and LTD stages under electrical stimulation.

(F) Type III: the LTD/LTD stimulated by combined pulses.

(G) Change trend of ΔG in LTP/LTD stages of type III.

(H) Combined pulse stimulation can regulate the nonlinearity and symmetry of LTP/LTD.

(I) Nonlinearity, symmetry, and update intervals for the type I, type II, and type III.

the fitting curve determines the sign and magnitude of the nonlinearity. The nonlinearity and ΔG affect the learning step of each training, which is also called the learning rate (Figure 3E).[42,43] The convex function (positive nonlinearity) causes the dynamic change of the learning step to weaken gradually. On the contrary, the concave function (negative nonlinearity) gradually enhances the learning step size. However, in the standard case, the learning step of the primary function (nonlinearity = 1) is a fixed value. Besides, the ΔG in the potentiation and depression process is analyzed to measure the signal-to-noise ratio (SNR) and learning step size for synaptic transistors (Figure S10). To explore the regulation of the optical pulse on nonlinearity and symmetry, type II and type III are developed. As depicted in Figure 3F, 20 optical pulses (red, green, and blue) are adopted in the potentiation stage, and 20 negative electric pulses (−0.5 V) are adopted in the depression

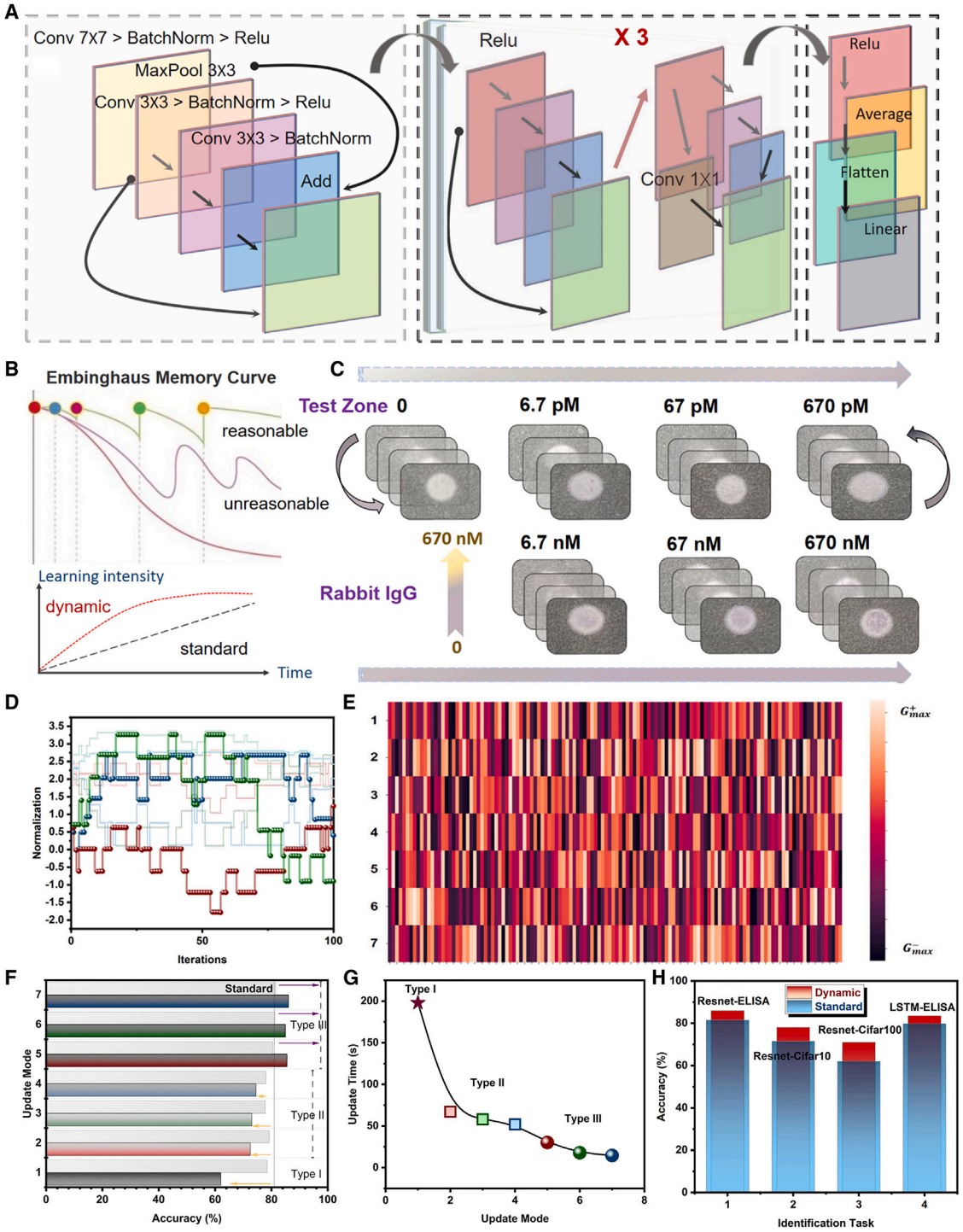

Figure 4. Residual neural network combines with dynamic update process to achieve immunological classification

(A) Block diagram of feedforward for the dynamic neuromorphic deep residual learning.

(B) Standard and dynamic learning rule based on Embinghaus memory.

(C) Image database of ELISA of seven rabbit IgG concentrations (0, 6.7 pM, 67 pM, 670 pM, 6.7 nM, 67 nM, and 670 nM).

(D) Trend of normalized dynamic learning step with the number of iterations.

(E) 7 × 128 wt matrix connects the last output layers.

Figure 4. *Continued*
(F) Accuracy of standard and dynamic conditions for three modulation modes.
(G) Update time during the ResNet neural network training process for type I, type II, and type III.
(H) Verification of the robustness of dynamic learning rules, which extend to the ResNet-ELISA, ResNet-Cifar10, ResNet-Cifar100, and LSTM-ELISA, respectively.

stage. Compared with type I, the symmetry defined as the ratio of $\Delta G_1/\Delta G_2$ is greatly improved in type II. ΔG_1 is the difference between the potentiation and depression stages (G^n_{LTP} and G^n_{LTD}) at the same level, and ΔG_2 is the difference between the two adjacent levels (G_n and G_{n-1}) of conductance. Furthermore, type III fundamentally solves the problem of insufficient symmetry based on the advantage of shortening the relaxation time.[44] Therefore, the three kinds of type III, which are composed of three optical pulses (red, green, and blue) and the same electrical pulse (0.5 V for LTP and −0.5 V for LTD), all have the excellent performance of symmetry as the result of the ratio of all $\Delta G_1/\Delta G_2$ floats within 2.1% (Figure 3G). To match higher learning efficiency in the ResNet (residual network) algorithm, the number of conductances that can be effectively utilized (N_{seff}) and the nonlinearity from 16 LTP/LTD curves are researched (Figure S7). Moreover, the ΔG between the two synaptic transistors (G^+ and G^-) is used to represent the weight range (−1 to 1) in the algorithm (Figure 3E). Notably, the left and right parts of the curve need to match the symmetry because the rising and falling stages of conductance should have one-to-one correspondence. To explore the regulation of optical pulse on nonlinearity and symmetry, type II and type III are developed (Figure 3H). To clearly show the modulation of three modes for updating rules, the parameters, including the nonlinearity, symmetry, and update interval, are analyzed to highlight the prominent advantage of applying type III (Figure 3I). Consequently, the ResNet of the neural network based on the dynamic learning rate according to the nonlinearity, symmetry, and update interval of the update rule is proposed for the classification task. To match the higher learning efficiency in the ResNet algorithm, the N_{seff} and nonlinearity from 16 LTP/LTD curves are researched (Figure S11).

Matching appropriate networks to enhance artificial intelligence application

To track the problem of deeper neural networks being more difficult to train, the ResNet with the residual learning framework is proposed to simplify the training of networks and gain accuracy from considerably increased depth. The degradation in the convergence process indicates that not all systems are similarly easy to optimize and can be solved by a deep residual learning framework (Figure 4A). The building block demonstrates that feedforward neural networks with shortcut connections can realize the formulation. Moreover, a backward neural network updates the synaptic weight layers with a dynamic learning rate according to the parameters extracted from the LTP/LTD curves.[45–47] Inspired by the Embinghaus memory map, dynamic learning rules are more in line with the memory behavior of biological synapses (Figure 4B). The ResNet contains a dynamic algorithm adopted to execute the classification task of ELISA for rabbit IgG. The collected data include the seven concentrations 0, 6.7 pM, 67 pM, 670 pM, 6.7 nM, 67 nM, and 670 nM (Figure 4C). The error of feedback part in the algorithm is based on the update rules measured by type III (electric pulse combined with blue light pulse). Compared with the standard case (lr = 0.1), the classification accuracy for seven rabbit IgGs is improved from 80.9% to 87.2% after 100 wt iterations. The influence of different colors of light in type III on the dynamic learning step shows the regulation ability of light (Figure 4D). Inspired by the first impression of human brain cognition, the dynamic learning rate makes the update step in the initial

epoch larger than in the later epoch of the training process because the LTP/LTD curve trend is a convex function.[48–52] Each output in the last layer is connected to 128 neurons, so Figure 4E shows the iterative updated 7 × 128 wt matrix. The complex disordered weight matrix proves that the weight value gradually differentiates into two extreme values (G_{max} and G_{min}) by relying on the Manhattan rule. To analyze the modulation effects of the three modes, the standard accuracy and dynamic accuracy under seven conditions (type I, type II_red, type II_green, type II_blue, type III_red, type III_green, and type III_blue are displayed (Figure 4F). On the one hand, the dynamic accuracy is higher than the standard accuracy in type III modulation due to the nonlinearity and excellent symmetry. On the other hand, the small update interval in type III shortens the whole iteration update time for the training process.[49–58] As shown in Figure 4G, the update times for red, green, and blue modes of type III are 11.6, 18.4, and 27.4 s, respectively. Consequently, the ResNet combined with characteristics can improve the classification compared with the standard situation and reduce the update time when the modulation mode type III is adopted. Furthermore, to verify the robustness of the dynamic learning rules in a similar deep neural network, the accuracy of different algorithm structures in identifying different classification tasks is compared (Figure 4H). The four neural networks and corresponding tasks are ResNet-ELISA, ResNet-Cifar10, ResNet-Cifar100, and LSTM-ELISA. Figure S12 demonstrates the operation speeds of Resnet-ELISA, Resnet-Cifar100, and the LSTM-ELISA through detailed training epochs. The recognition rate is not significantly affected by the initial weight when the random floating value is smaller than the learning step in a random process (Figure S13). The database of Cifar10 and Cifar100 and the results of verifying robustness explicitly demonstrate the feasibility of a dynamic learning rate (Figure S14). The obvious result is that the above neural networks with dynamic learning rate strength enhance the classification ability (the average improved accuracy is 6.8%).

In conclusion, this work demonstrates the Al/InOx/MXenes/ZrOx-Li/Si/Al structure as bionic retina and proposes a dynamic learning strategy for the recognition of ELISA_IgG in immunology. PPF, STP/LTP, and EPSC are the basic information flows, as is the typical manifestation of synaptic plasticity. Here, we analyze the dynamic learning rate, the update interval, and the learning accuracy rate according to various LTP/LTD curves that were regulated separately by three modulation modes (type I, type II, and type III). The synaptic devices stimulated by type III have high linearity and symmetry, which are necessary to reduce the number of training epochs in the neural network. At the same time, the fast conductance recovery trend can reduce the interval of each calculation. Moreover, the rabbit IgG of ELISA is used to demonstrate the detection potential in immunology and other neural networks (LSTM) composed of the Cifar10 and Cifar100 database are then developed to verify the robustness and feasibility of dynamic learning rule. The synaptic transistor based on two-dimensional materials and a dynamic learning strategy enriches the weight update process of neural morphological systems and further develops bionic retina to successfully complete complex visual perception tasks.

EXPERIMENTAL PROCEDURES

Resource availability

Lead contact

Further information and requests for resources should be directed to and will be fulfilled by the lead contact, Chun Zhao (chun.zhao@xjtlu.edu.cn).

Materials availability

This study did not generate new unique materials. The full details of the experiments and materials are provided in the experimental procedures.

Data and code availability

This study did not generate any new code. The authors declare that the data supporting the findings of this study are available within the article and the supplemental information.

Synthesis of transistors

The ZrO_x precursor solution was obtained by dissolving 1.5 M aluminum nitrate hydrate ($Zr(NO_3)_2 \cdot xH_2O$) in 20 mL 2-methoxy ethanol (2-Me). ZrO_x-Li precursor solution was obtained by mixing 1.5 M aluminum nitrate hydrate ($Zr(NO_3)_2 \cdot xH_2O$) and 0.15 M indium nitrate hydrate with 20 mL deionized water. The InO_x precursor solution was obtained by dissolving indium nitrate hydrate ($In(NO_3)_3 \cdot xH_2O$) into 20 mL deionized water. All solutions were vigorously stirred under atmospheric conditions for 5 h and filtered before spin coating using 0.25 μm polytetrafluoroethylene (PTFE) syringe filters, respectively. To prepare MXenes, first, 2 g lithium fluoride (LiF) with 99.99% metal basis from Aladdin and 40 mL hydrochloric acid (HCl) with a concentration of 36%–38% from Sinopharm Chemical Reagent were mixed and stirred in a PTFE beaker for 30 min. Next, 2 g titanium aluminum carbide MAX (MAX-Ti3AlC2) with a purity of 98% from 11 Technology was gradually added to the beaker under continuous stirring, and the reaction temperature was maintained at 35°C for 24 h in a fume hood. After the reaction was completed, the resulting solution was centrifuged for 10 min at 3,500 rpm, and the supernatant was discarded. Then, 40 mL deionized (DI) water was added to the sediment in the centrifuge tubes, and the tubes were manually shaken to mix the sediment with the DI water. The mixture was further ultrasonicated for 15 min using a high-power ultrasonic machine with 750 W output. These centrifugation and ultrasonication steps were repeated until the pH of the supernatant reached 5. Subsequently, 40 mL ethanol (CH_3CH_2OH) with a purity of 99.7% from Sinopharm Chemical Reagent was added to the centrifuge tubes, and the mixture was ultrasonicated for 1.5 h using an intercalator function. Then, the mixture was centrifuged at 10,000 rpm for 10 min, and 20 mL DI water was added to the sediment. The mixture was further ultrasonicated for 20 min and then centrifuged again at 3,500 rpm for 3 min to obtain a black-brown few-layer dispersion with a concentration of approximately 5 mg mL^{-1}. Finally, the MXene dispersion was stored in an argon atmosphere, and the storage time was limited to 14 days.

Fabrication of synaptic transistors

First, a heavily doped Si (n^{++}) substrate was cleaned by DI water and dried under N_2 flow. Afterward, the processed substrate was further treated by plasma for 15 min to make the film surface hydrophilic. The ZrO_x and ZrO_x-Li films were spin cast with precursor solution at 4,500 rpm for 30 s and then annealed for 80 min at 250°C in air atmosphere. Then, the MXene solution was diluted to 1 mg/mL and spin coated at 3,000 rpm for 20 s on the surfaces of the ZrO_x and ZrO_x-Li films. Substrates with solution film were then oxidized at 80°C for 1 min on a hotplate in air conditions. The InO_x film was spin cast with precursor solution at 3,500 rpm for 30 s and then annealed for 1 h at 200°C in air atmosphere. The 30-nm-thick Al source/drain (S/D) electrodes were fabricated by thermal evaporation through the shadow mask.

ELISA detection

Rabbit IgG is the most common model sensing target in c-ELISAs, and a schematic of the direct c-ELISA protocol for rabbit IgG on our multiwell μPAD is shown in

Figure 1B. Typically, a direct c-ELISA is carried out in six steps: (1) biofunctionalizing the test zone using periodate potassium; (2) immobilizing the rabbit IgG antigen on the test zone; (3) blocking the test zone to prevent nonspecific adsorption of rabbit IgG proteins; (4) labeling the immobilized rabbit IgG antigen with ALP-conjugated anti-rabbit IgG antibody; (5) washing away the unbound antibody using PBS buffer; and (6) adding the BCIP/NBT substrate.

Characterization

A semiconductor parameter analyzer (Agilent B1500) with transistor characterization software under atmospheric conditions was operated to test the electrical properties of the Al/InOx/MXenes/ZrOx-Li/Si/Al synaptic transistor. In order to measure the EPSC and LTD/LTP current flowing between the S/D electrodes, a 0.1 V steady voltage bias was applied to the postsynaptic terminal (V_{post}).[59,60] The chemical compositions of dielectric and semiconductor layers were measured by X-ray photoelectric spectroscopy (XPS). The crystallization and structural information of the thin films was displayed using X-ray diffraction (XRD; BRUKER D8 ADVANCE) with Cu Kα radiation (λ = 1.542 Å).

ResNet simulation

We use the ResNet as the base model. After we convert the image data into RGB three-channel matrix data, we could directly pass them into the residual block. The residual block is the main component of ResNet. Compared with the ordinary neural network structure, the residual block could not only perform weighted operations through the convolution layer and activation function mechanism to extract features but could also retain the initial information of the input data and fuse it with the obtained feature information. Two residual blocks and one linear layer are used in our model. The input image data are passed through two residual blocks to complete the feature extraction and then passed to the linear layer to complete the final classification task. Usually, this is a complete ResNet workflow, and we use a dynamic learning rate in the training step. After each training of the network, different learning steps are used to update the network parameters according to the change direction of the loss.[55–60]

The calculated conductance of synaptic transistors in the crossbar array was applied with the positive synaptic weight value. The measurement of the neurocomputing in ResNet includes negative values.[50] Subsequently, the synaptic weight ($W = G^+ - G^-$) was expressed as the difference between the state of two synaptic devices (expressed as G^+ and G^-) between each conductance value. The initial weights were set up randomly to fluctuate near 0, and the value between G_{min} and G_{max} was normalized to (−1,1). The actual changed value of weight updating depends on the difference between the conductance state of two synaptic devices (G^+ and G^-), which is extracted from the LTP/LTD curve. The change of single synaptic weight is defined as the ΔG in two synaptic transistors. When sgn(ΔW) >0, the formula $W\uparrow = G^+\uparrow\text{-}G^-\downarrow$ will be used, and when sgn(ΔW) <0, $W\downarrow = G^+\downarrow\text{-}G^-\uparrow$ will be used.

In order to make the model converge earlier, we use two functions to adjust the learning rate dynamically. After each round of training, we conducted a round of tests to test the model's performance. If the error of classification of the current round is smaller than that of the previous round, we use the function $[e^* (e + 1)]^{½}$ to appropriately increase the learning rate, where e is the number of training rounds to adjust the value of the learning rate. If the classification error of the current round

is more significant than that of the previous round, we use the function e*1/(e + 1) to reduce the learning rate appropriately.

SUPPLEMENTAL INFORMATION

Supplemental information can be found online at https://doi.org/10.1016/j.xcrp.2023.101481.

ACKNOWLEDGMENTS

This research was funded in part by the National Natural Science Foundation of China (62204210), the Natural Science Foundation of Jiangsu Province (BK20220284), the Natural Science Foundation of the Higher Education Institutions of Jiangsu Province (22KJB510013), the Natural Science Foundation of the Jiangsu Higher Education Institutions of China Program (19KJB510059), the Suzhou Science and Technology Development Planning Project: Key Industrial Technology Innovation (SYG201924), University Research Development Fund (RDF-17-01-13), and the Key Program Special Fund in XJTLU (KSF-T-03, KSF-A-07). This work was partially supported by the XJTLU AI University Research Centre and Jiangsu (Provincial) Data Science and Cognitive Computational Engineering Research Centre at XJTLU and Jiangsu Key Laboratory for Carbon-based Functional Materials & Devices, Soochow University.

AUTHOR CONTRIBUTIONS

Q.W., P.S., W.L., and C.Z. conceived and oversaw the project. S.D. and Y.S. fabricated the MXenes and c-ELISAs. Q.W. and S.W. fabricated the devices and performed the electrical test. J.G., L.Y., and H.G. operated material characterizations. Q.W. and J.Q. programmed codes for image processing. Q.W. analyzed the results and wrote the manuscript. P.S., W.L., and C.Z. offered resources for the experiments. All authors provided input during manuscript preparation and revisions.

DECLARATION OF INTERESTS

The authors declare no competing interests.

Received: January 12, 2023
Revised: April 16, 2023
Accepted: June 9, 2023
Published: June 30, 2023

REFERENCES

1. Lin, P., Li, C., Wang, Z., Li, Y., Jiang, H., Song, W., Rao, M., Zhuo, Y., Upadhyay, N.K., Barnell, M., et al. (2020). Three-dimensional memristor circuits as complex neural networks. Nat. Electron. *3*, 225–232.

2. Ham, D., Park, H., Hwang, S., and Kim, K. (2021). Neuromorphic electronics based on copying and pasting the brain. Nat. Electron. *4*, 635–644.

3. Sun, Y., Ding, Y., and Xie, D. (2021). Mixed-dimensional van der Waals heterostructures enabled optoelectronic synaptic devices for neuromorphic applications. Adv. Funct. Mater. *31*, 2105625.

4. Liu, L., Li, Y., Huang, X., Chen, J., Yang, Z., Xue, K.H., Xu, M., Chen, H., Zhou, P., and Miao, X. (2021). low-power memristive logic device enabled by controllable 508 oxidation of 2D HfSe2 for in-memory computing. Adv. Sci. *8*, 2005038.

5. Yang, C.S., Shang, D.S., Liu, N., Fuller, E.J., Agrawal, S., Talin, A.A., Li, Y.Q., Shen, B.G., and Sun, Y. (2018). All-Solid-state synaptic transistor with ultralow conductance for neuromorphic computing. Adv. Funct. Mater. *28*, 1804170.

6. Hoffman, J., Pan, X., Reiner, J.W., Walker, F.J., Han, J.P., Ahn, C.H., and Ma, T.P. (2010). Ferroelectric field effect transistors for memory application. Adv. Mater. *22*, 2957–2961.

7. Sun, J., Oh, S., Choi, Y., Seo, S., Oh, M.J., Lee, M., Lee, W.B., Yoo, P.J., Cho, J.H., and Park, J.-H. (2018). Optoelectronic synapse based on IGZO-alkylated graphene oxide hybrid structure. Adv. Funct. Mater. *28*, 1804397.

8. Wan, C., Cai, P., Guo, X., Wang, M., Matsuhisa, N., Yang, L., Lv, Z., Luo, Y., Loh, X.J., and Chen, X. (2020). An artificial sensory neuron with visual-haptic fusion. Nat. Commun. *11*, 4602.

9. Meng, J., Wang, T., Zhu, H., Ji, L., Bao, W., Zhou, P., Chen, L., Sun, Q.Q., and Zhang, D.W. (2022). Integrated in-sensor computing optoelectronic device for environment-adaptable artificial retina perception application. Nano Lett. *22*, 81–89.

10. Tan, H., Zhou, Y., Tao, Q., Rosen, J., and van Dijken, S. (2021). Bioinspired multisensory neural network with crossmodal integration and recognition. Nat. Commun. *12*, 1120.

11. Lu, K., Li, X., Sun, Q., Pang, X., Chen, J., Minari, T., Liu, X., and Song, Y. (2021).

Solutionprocessed electronics for artificial synapses. Mater. Horiz. *8*, 447–470.

12. Kim, M.K., and Lee, J.S. (2019). Ferroelectric analog synaptic transistors. Nano Lett. *19*, 2044–2050.

13. Bisri, S.Z., Shimizu, S., Nakano, M., and Iwasa, Y. (2017). Endeavor of iontronics: from fundamentals to applications of ion-controlled electronics. Adv. Mater. *29*, 1607054.

14. Kim, S., Choi, B., Lim, M., Yoon, J., Lee, J., Kim, H.D., and Choi, S.J. (2017). Pattern recognition using carbon nanotube synaptic transistors with an adjustable weight update protocol. ACS Nano *11*, 2814–2822.

15. Lv, Z., Chen, M., Qian, F., Roy, V.A.L., Ye, W., She, D., Wang, Y., Xu, Z.X., Zhou, Y., and Han, S.T. (2019). Mimicking neuroplasticity in a hybrid biopolymer transistor by dual modes modulation. Adv. Funct. Mater. *29*, 1902374.

16. Zhang, C., Wang, S., Zhao, X., Yang, Y., Tong, Y., Zhang, M., Tang, Q., and Liu, Y. (2021). Sub-Femtojoule-energy-consumption conformable synaptic transistors based on organic single-crystalline nanoribbons. Adv. Funct. Mater. *31*, 2007894.

17. Wang, Y., Liao, Q., She, D., Lv, Z., Gong, Y., Ding, G., Ye, W., Chen, J., Xiong, Z., Wang, G., et al. (2020). Modulation of binary neuroplasticity in a heterojunction-based ambipolar transistor. ACS Appl. Mater. Interfaces *12*, 15370–15379.

18. Yin, L., Huang, W., Xiao, R., Peng, W., Zhu, Y., Zhang, Y., Pi, X., and Yang, D. (2020). Optically stimulated synaptic devices based on the hybrid structure of silicon nanomembrane and perovskite. Nano Lett. *20*, 3378–3387.

19. Park, H.L., Kim, H., Lim, D., Zhou, H., Kim, Y.H., Lee, Y., Park, S., and Lee, T.W. (2020). Retina-inspired carbon nitride-based photonic synapses for selective detection of UV light. Adv. Mater. *32*, 1906899.

20. Lee, Y., and Lee, T.W. (2019). Organic synapses for neuromorphic electronics: from brain-inspired computing to sensorimotor nervetronics. Acc. Chem. Res. *52*, 964–974.

21. Gubala, V., Harris, L.F., Ricco, A.J., Tan, M.X., and Williams, D.E. (2012). Point of care diagnostics: status and future. Anal. Chem. *84*, 487–515.

22. Yager, P., Domingo, G.J., and Gerdes, J. (2008). Point-of-care diagnostics for global health. Annu. Rev. Biomed. Eng. *10*, 107–144.

23. Nayak, S., Blumenfeld, N.R., Laksanasopin, T., and Sia, S.K. (2017). Point-of-care diagnostics: recent developments in a connected age. Anal. Chem. *89*, 102–123.

24. Rivas, L., Medina-Sánchez, M., de la Escosura-Muñiz, A., and Merkoçi, A. (2014). Improving sensitivity of gold nanoparticle-based lateral flow assays by using wax-printed pillars as delay barriers of microfluidics. Lab Chip *14*, 4406–4414.

25. Cate, D.M., Adkins, J.A., Mettakoonpitak, J., and Henry, C.S. (2015). Recent developments in paper-based microfluidic devices. Anal. Chem. *87*, 19–41.

26. Yu, J., Ge, L., Huang, J., Wang, S., and Ge, S. (2011). Microfluidic paper-based chemiluminescence biosensor for simultaneous determination of glucose and uric acid. Lab Chip *11*, 1286–1291.

27. Wang, M., Song, Z., Jiang, Y., Zhang, X., Wang, L., Zhao, H., Cui, Y., Gu, F., Wang, Y., and Zheng, G. (2021). A three-dimensional pinwheel-shaped paper-based microfluidic analytical device for fluorescence detection of multiple heavy metals in coastal waters by rational device design. Anal. Bioanal. Chem. *413*, 3299–3313.

28. Cheng, C.-M., Martinez, A.W., Gong, J., Mace, C.R., Phillips, S.T., Carrilho, E., Mirica, K.A., and Whitesides, G.M. (2010). Paper-based ELISA. Angew. Chem. Int. Ed. Engl. *49*, 4771–4774.

29. Alibart, F., Pleutin, S., Guérin, D., Novembre, C., Lenfant, S., Lmimouni, K., Gamrat, C., and Vuillaume, D. (2010). An organic nanoparticle transistor behaving as a biological spiking synapse. Adv. Funct. Mater. *20*, 330–337.

30. Li, Y., Xuan, Z., Lu, J., Wang, Z., Zhang, X., Wu, Z., Wang, Y., Xu, H., Dou, C., Kang, Y., et al. (2021). One transistor one electrolyte-gated transistor based spiking neural network for power-efficient neuromorphic computing system. Adv. Funct. Mater. *31*, 2100042.

31. Choi, Y., Kim, J.H., Qian, C., Kang, J., Hersam, M.C., Park, J.H., and Cho, J.H. (2020). Gate-Tunable synaptic dynamics of ferroelectric-coupled carbon-nanotube transistors. ACS Appl. Mater. Interfaces *12*, 4707–4714.

32. Cohen-Cory, S. (2002). The developing synapse: construction and modulation of synaptic structures and circuits. Science *298*, 770–776.

33. Seo, S., Kang, B.-S., Lee, J.-J., Ryu, H.-J., Kim, S., Kim, H., Oh, S., Shim, J., Heo, K., and Oh, S. (2020). Artificial van der Waals hybrid synapse and its application to acoustic pattern recognition. Nat. Commun. *11*, 3936.

34. Li, E., Gao, C., Yu, R., Wang, X., He, L., Hu, Y., Chen, H., Chen, H., and Guo, T. (2022). MXene based saturation organic vertical photoelectric transistors with low subthreshold swing. Nat. Commun. *13*, 2898.

35. Liu, Y., Liu, D., Gao, C., Zhang, X., Yu, R., Wang, X., Li, E., Hu, Y., Guo, T., and Chen, H. (2022). Self-powered high-sensitivity all-in-one vertical tribo-transistor device for multi-sensing-memory-computing. Nat. Commun. *13*, 7917.

36. Zhang, X., Wu, S., Yu, R., Li, E., Liu, D., Gao, C., Hu, Y., Guo, T., and Chen, H. (2022). Programmable neuronal-synaptic transistors based on 2D MXene for a high-efficiency neuromorphic hardware network. Matter *5*, 3023–3040.

37. Wang, C., Liang, S.-J., Wang, C.-Y., Yang, Z.-Z., Ge, Y., Pan, C., Shen, X., Wei, W., Zhao, Y., Zhang, Z., et al. (2021). Scalable massively parallel computing using continuous-time data representation in nanoscale crossbar array. Nat. Nanotechnol. *16*, 1079–1085.

38. Yu, J., Gao, G., Huang, J., Yang, X., Han, J., Zhang, H., Chen, Y., Zhao, C., Sun, Q., and Wang, Z.L. (2021). Contact-electrification-activated artificial afferents at femtojoule energy. Nat. Commun. *12*, 1581.

39. Yang, C.S., Shang, D.S., Liu, N., Shi, G., Shen, X., Yu, R.C., Li, Y.Q., and Sun, Y. (2017). A synaptic transistor based on quasi-2D molybdenum oxide. Adv. Mater. *29*, 1700906.

40. Zhao, T., Zhao, C., Xu, W., Liu, Y., Gao, H., Mitrovic, I.Z., Lim, E.G., Yang, L., and Zhao, C.Z. (2021). Bio-inspired photoelectric artificial synapse based on two-dimensional Ti3C2Tx MXenes floating gate. Adv. Funct. Mater. *31*, 2106000.

41. Li, B., Liu, Y., Wan, C., Liu, Z., Wang, M., Qi, D., Yu, J., Cai, P., Xiao, M., and Zeng, Y. (2018). Mediating short-term plasticity in an Artificial memristive synapse by the orientation of silica mesopores. Adv. Mater. *30*, 1706395.

42. Lee, M., Lee, W., Choi, S., Jo, J.W., Kim, J., Park, S.K., and Kim, Y.H. (2017). Brain-inspired photonic neuromorphic devices using photodynamic amorphous oxide semiconductors and their persistent photoconductivity. Adv. Mater. *29*, 1700951.

43. Boyn, S., Grollier, J., Lecerf, G., Xu, B., Locatelli, N., Fusil, S., Girod, S., Carrétéro, C., Garcia, K., Xavier, S., et al. (2017). Learning through ferroelectric domain dynamics in solid-state synapses. Nat. Commun. *8*, 14736.

44. Li, H.K., Chen, T.P., Liu, P., Hu, S.G., Liu, Y., Zhang, Q., and Lee, P.S. (2016). A light-stimulated synaptic transistor with synaptic plasticity and memory functions based on InGaZnOx–Al2O3 thin film structure. J. Appl. Phys. *119*, 244505.

45. Hao, D., Zhang, J., Dai, S., Zhang, J., and Huang, J. (2020). Perovskite/organic SemiconductorBased photonic synaptic transistor for artificial visual system. ACS Appl. Mater. Interfaces *12*, 39487–39495.

46. Li, J., Yang, Y.-H., Chen, Q., Zhu, W.-Q., and Zhang, J.-H. (2020). Aqueous-solution-processed proton-conducting carbon nitride/polyvinylpyrrolidone composite electrolytes for low-power synaptic transistors with learning and memory functions. J. Mater. Chem. C *8*, 4065–4072.

47. Yang, J.T., Ge, C., Du, J.Y., Huang, H.Y., He, M., Wang, C., Lu, H.B., Yang, G.Z., and Jin, K.J. (2018). Artificial synapses emulated by an electrolyte-gated tungsten-oxide transistor. Adv. Mater. *30*, 1801548.

48. Li, J., Jiang, D., Yang, Y., Zhou, Y., Chen, Q., and Zhang, J. (2020). Li-Ion doping as a strategy to modulate the electrical-double-layer for improved memory and learning behavior of synapse transistor based on fully aqueous-solution-processed In2O3/AlLiO film. Adv. Electron. Mater. *6*, 1901363.

49. Dai, S., Zhao, Y., Wang, Y., Zhang, J., Fang, L., Jin, S., Shao, Y., and Huang, J. (2019). Recent advances in transistor-based artificial synapses. Adv. Funct. Mater. *29*, 1903700.

50. Du, J., Xie, D., Zhang, Q., Zhong, H., Meng, F., Fu, X., Sun, Q., Ni, H., Li, T., Guo, E.-j., et al. (2021). A robust neuromorphic vision sensor with optical control of ferroelectric switching. Nano Energy *89*, 106439.

51. Buscema, M., Island, J.O., Groenendijk, D.J., Blanter, S.I., Steele, G.A., van der Zant, H.S.J., and Castellanos-Gomez, A. (2015). Photocurrent generation with two-dimensional

van der Waals semiconductors. Chem. Soc. Rev. *44*, 3691–3718.

52. Lyu, B., Choi, Y., Jing, H., Qian, C., Kang, H., Lee, S., and Cho, J.H. (2020). 2D MXene–TiO2 core–shell nanosheets as a data-storage medium in memory devices. Adv. Mater. *32*, 1907633.

53. Xu, B., Zhu, M., Zhang, W., Zhen, X., Pei, Z., Xue, Q., Zhi, C., and Shi, P. (2016). Ultrathin MXene-micropattern-based field-effect transistor for probing neural activity. Adv. Mater. *28*, 3333–3339.

54. Zhang, C.J., Ma, Y., Zhang, X., Abdolhosseinzadeh, S., Sheng, H., Lan, W., Pakdel, A., Heier, J., and Nüesch, F. (2020). Two-dimensional transition metal carbides and nitrides (MXenes): synthesis, properties, and electrochemical energy storage applications. Energy Environ. Mater. *3*, 29–55.

55. He, Y., Zhu, L., Zhu, Y., Chen, C., Jiang, S., Liu, R., Shi, Y., and Wan, Q. (2021). Recent progress on emerging transistor-based neuromorphic devices. Adv. Intell. Syst. *3*, 2000210.

56. Han, H., Xu, Z., Guo, K., Ni, Y., Ma, M., Yu, H., Wei, H., Gong, J., Zhang, S., and Xu, W. (2020). Tunable synaptic plasticity in crystallized conjugated polymer nanowire artificial synapses. Adv. Intell. Syst. *2*, 1900176.

57. Kwon, S.M., Cho, S.W., Kim, M., Heo, J.S., Kim, Y.H., and Park, S.K. (2019). Environment-adaptable artificial visual perception behaviors using a light - adjustable optoelectronic neuromorphic device array. Adv. Mater. *31*, 1906433.

58. Han, J.-K., Geum, D.-M., Lee, M.-W., Yu, J.-M., Kim, S.K., Kim, S., and Choi, Y.-K. (2020). Bioinspired photoresponsive single transistor neuron for a neuromorphic visual system. Nano Lett. *20*, 8781–8788.

59. Hong, S., Cho, H., Kang, B.H., Park, K., Akinwande, D., Kim, H.J., and Kim, S. (2021). Neuromorphic active pixel image sensor array for visual memory. ACS Nano *15*, 15362–15370.

60. Li, L., Wang, X.-L., Pei, J., Liu, W.-J., Wu, X., Zhang, D.W., and Ding, S.-J. (2020). Floating gate photosensitive synaptic transistors with tunable functions for neuromorphic computing. Sci. China Mater. *76*, 1219–1230.